


M. Rezaiee-Pajand  · E. Arabi · Amir R. Masoodi

A triangular shell element for geometrically nonlinear analysis

Received: 31 December 2016 / Revised: 26 July 2017 / Published online: 26 September 2017
© Springer-Verlag GmbH Austria 2017

Abstract In this paper, a geometrically nonlinear formulation for a six-node triangular shell element is proposed. Total Lagrangian formulation is utilized to consider large displacements and rotations in the shell analysis. To avoid shear and membrane locking, a proper interpolation function for the strain field is implemented. Both algorithm and flowchart of the nonlinear solution, which are utilized in the author's computer program, are presented. To validate the suggested formulation, several popular benchmark problems are solved. Moreover, the obtained results are compared with those of the other well-known elements. Findings demonstrate the ability of the suggested shell element.

List of symbols

a_i	The thickness of node i
B_{ij}	The linear strain–displacement matrix
e_{ij}	Linear part of strain tensor
e_1, e_2, e_3	The unit vector in global Cartesian system
$h_i(r, s, t)$	The two-dimensional interpolation functions
N_{ij}	The nonlinear strain–displacement matrix
Q^i	Rotation matrix
r, s, t	The convected coordinates
\vec{u}	The nodal displacement vector in global Cartesian system
\vec{U}	Vector of incremental nodal displacements
u, v, w	The nodal displacements
\vec{u}_l	The linear part of nodal displacement
\vec{u}_q	The quadratic part of nodal displacement
\vec{V}_1^i, \vec{V}_2^i	The unit vectors orthogonal to V_n^i and to each other
\vec{V}_n^i	The director vector of node i
\vec{x}_i	The position vector of node i
α_i, β_i	The rotation of V_n^i about V_1^i, V_2^i
ε_{ij}	Green–Lagrange strain tensor
η_{ij}	Nonlinear part of strain tensor

1 Introduction

The geometrically nonlinear behavior of shell structures has played an important role in the mechanical and structural engineering fields. Based on this fact, it is essential to employ an appropriate computational method that can accurately predict the nonlinear deformations and stresses in shell structure. So far, several miscellaneous models for nonlinear analysis of shells have been developed by many researchers.

Most of the studies on the nonlinear analysis of shells have utilized the finite element method. Basically, four types of elements are employed in this analysis: combination of plate bending and plane stress element, solid 3D element, degenerated shell element, and a 2D element based on a shell theory [1]. It should be added that the last two types are the most common procedures to analyze the shell structures. For the first time, a general formulation based on the degenerated shell element theory for the curved and thick shell elements was obtained by Ahmad et al. [2]. They used a simplified form for axisymmetric cases, such as the first-order shear deformation theory. The research of Hughes and Liu [3,4], Hughes and Carnoy [5], Bathe and Dvorkin [6], Parks and Stanley [7], and Liu et al. [8] among many other studies represented the same methodology for analyzing the shell structures. In 1986, a new nine-node degenerated shell element was developed by Huang and Hinton [9]. They employed an enhanced interpolation of the shear strains to overcome the shear locking problem. In another work, nonlinear shell analysis was performed based on the degenerated iso-parametric shell element by Hsiao and Chen [10]. They tested their solution by a finite rotation method. Moreover, the thesis of Stanley [11] and the books of Bathe [12] and Crisfield [13] represented the generalities of the degenerated shell element procedure with some numerical examples.

A 2D element based on a shell theory was first used by Simo and Fox [14]. They illustrated that using classical shell theory along with one-director Cosserat surface leads to efficient numerical formulations. Some of the problems solved by this method can be found in [15–17]. In addition, a general shell element was developed by Bathe and Dvorkin [18]. They used the Mixed Interpolation of Tensorial Components (MITC) method and proposed a new eight-node shell element. Furthermore, nonlinear analysis of shell structures based on this scheme was performed by Dvorkin [19]. In his study, three elements were examined under the restriction of small and finite strains in the elasto-plastic analyses of shells. The mentioned technique was completely described in the theses of Dvorkin [20], Lee [21], and Bathe's books [12,22].

In the last decades, the MITC method was widely used to develop triangular shell elements for linear and nonlinear analyses. In 2004, an isotropic triangular shell finite element based on this approach was proposed by Lee and Bathe [23]. They formulated several triangular shell elements based on this method. Moreover, the characteristics of convergence for some 3-node shell finite elements, developed based on the MITC approach, were studied by Lee et al. [24]. They investigated the effects of element isotropy and mesh patterns on the convergence rate of MITC triangular shell elements. Furthermore, a finite element computational model for the nonlinear analysis of shell structures was proposed by Arciniega and Reddy [1]. The tensorial-based formulation was employed to describe the mathematical model of a shell element in curvilinear coordinates. It should be added that a family of higher-order elements with Lagrangian interpolations was utilized to avoid the shear and membrane locking. In order to improve the performance of MITC3 shell element, Lee et al. [25] implemented the Hellinger–Reissner (HR) variational principle in the framework of MITC element. They also proposed a new approximated transverse shear strain field. Moreover, a six-node triangular element based on the MITC approach was presented by Kim and Bathe [26]. They investigated the convergence behavior of the element in membrane and bending-dominated benchmark problems. Furthermore, new strain interpolation functions were proposed.

Recently, Jeon et al. [27] presented a new scheme to improve the MITC3 element. They used cover functions to interpolate the strain fields. The suggested approach increased the accuracy of solution effectively, without any traditional local mesh refinement. Another research was performed on a triangular MITC element by Lee et al [28]. In addition, they proposed a new triangular shell element entitled MITC3+ with an additional bubble node. They used cubic bubble functions for rotational degrees of freedom. It should be added that new transverse shear strain interpolations were used in the formulation. In another paper, the geometrically nonlinear analysis of shell structures was performed by Jeon et al. [29]. They extended the formulation of MITC3+ shell element to study the nonlinear behavior of shells. The total Lagrangian formulation was employed for large displacements and rotations. They verified the accuracy of the proposed element by solving several nonlinear benchmark problems.

Some studies were carried out pertaining to the computational methods in linear and nonlinear analyses of shell structures. Among them, an investigation of interactive-adaptive methods for nonlinear FE structural analysis was performed by Mathisen and Okstad [30]. Furthermore, a solid-shell FE model was implemented

into the ABAQUS software as a user-defined element by Li et al. [31]. They simulated the sheet-metal-forming processes through this software. In another study, a fully automated high-order hexahedral mesh generation algorithm was proposed by Sorger et al. [32] based on enhanced sweeping methods for shell structures. Moreover, a technique was presented by Areias et al. [33] to improve the quadrilateral shell element. Their analysis was performed in both out-of-plane and in-plane bending cases. In their research, a mixed formulation was employed. On the other hand, a smoothed particle hydrodynamics (SPH) method was employed for large deformation analysis of curved shells by Zhang et al. [34]. Their formulation was based on the total Lagrangian. Moreover, a nonlinear bending analysis of plates and cylindrical shells was performed by Nguyen-Van et al. [35]. They utilized a flat four-node element based on the finite von Kármán large deflection formulation and total Lagrangian scheme. Avramov [36] investigated the nonlinear modes of vibration for cylindrical shells. The geometrical nonlinearity was incorporated into his research. He utilized the Galerkin method to solve the partial differential equations. In another research, Eliseev and Vetyukov employed the principle of virtual work to formulate a shell element having 5 degrees of freedom [37]. To transform the relations to the reference configuration, they presented a new formulation for Piola tensors.

A variety of formulations and theories have been employed for the geometrically nonlinear analysis of shell structures so far. For instance, a total Lagrangian displacement-based formulation was proposed by Pai [38] who considered shells under large displacements and rotations. Taking into account thickness strains, a quadrilateral mixed hybrid shell element was developed by Klinkel et al. [39]. They utilized a nonlinear 3D constitutive equation. In another research, Velicic [40] used Γ -convergence and nonlinear three-dimensional elasticity to solve the shallow shells. Furthermore, the geometrically nonlinear theory of 6-parametric elastic shells with drilling degrees of freedom was proposed by Birsan and Neff [41]. In 2013, Pruchnicki employed a simplified theory based on the thickness-wise expansion of the potential energy truncated at third order along the thickness [42]. Also, he approximated the displacement field through the thickness of a shell by a fifth-order Taylor-Young expansion. In his research, the model was derived from the truncation of the potential energy at fifth order [43]. In addition, an isotropic spherical shell subject to uniform external pressure and concentrated load was analyzed by Evkin et al. [44]. Another study was performed for the buckling load of closed elastic isotropic shallow conical shells under the effect of initial imperfection by Karasev [45]. Based on the absolute nodal coordinate formulation (ANCF), a three-dimensional nonlinear finite element analysis of on Euler–Bernoulli thin beam was developed by Nachbagauer et al. [46]. Since they updated the directors during analysis, no singularities occurred in their process.

According to the literature, the MITC methods have been widely used to develop a lot of shell elements. Recently, a new element, called MITC6, was proposed only for the linear analysis of shells by Kim and Bathe [26]. In this paper, the nonlinear formulation for this element is presented. The element has generally thirty degrees of freedom. To consider large displacements and rotations in the shell analysis, the total Lagrangian formulation is employed. To avoid shear locking, appropriate strain field interpolation functions are used. In order to utilize this six-node triangular element in the geometric nonlinear analysis, a computer program is developed by the authors. Both algorithm and flowchart of the nonlinear analysis, which are exploited in this program, are presented. To validate the suggested formulation, several popular benchmark problems are solved. Moreover, the results are compared with the other well-known elements. The numerical outcomes reveal the versatility of the proposed element.

2 Displacement field

In this Section, the incremental displacement for the six-node triangular shell element is presented. Each node has five degrees of freedom, including three transitional degrees of freedom and two rotations. The total Lagrangian formulation is employed for large displacements and rotations. This element has three corners and three mid-side nodes. In the suggested equations, a superscript and also subscript t are used to show load step and configuration. It is assumed that the director vector of nodes stays straight during deformation. Moreover, the other simplified assumption is about the thickness of the element remaining invariant along the director vector. The geometric configuration of the proposed shell element, at time t , is shown in Fig. 1.

The geometry of the six-node triangular shell element is as follows:

$${}^t \vec{x}(r, s, t) = \sum_{i=1}^6 h_i(r, s) {}^t \vec{x}_i + \frac{t}{2} \sum_{i=1}^6 a_i h_i(r, s) {}^t \vec{V}_n^i, \quad (1)$$

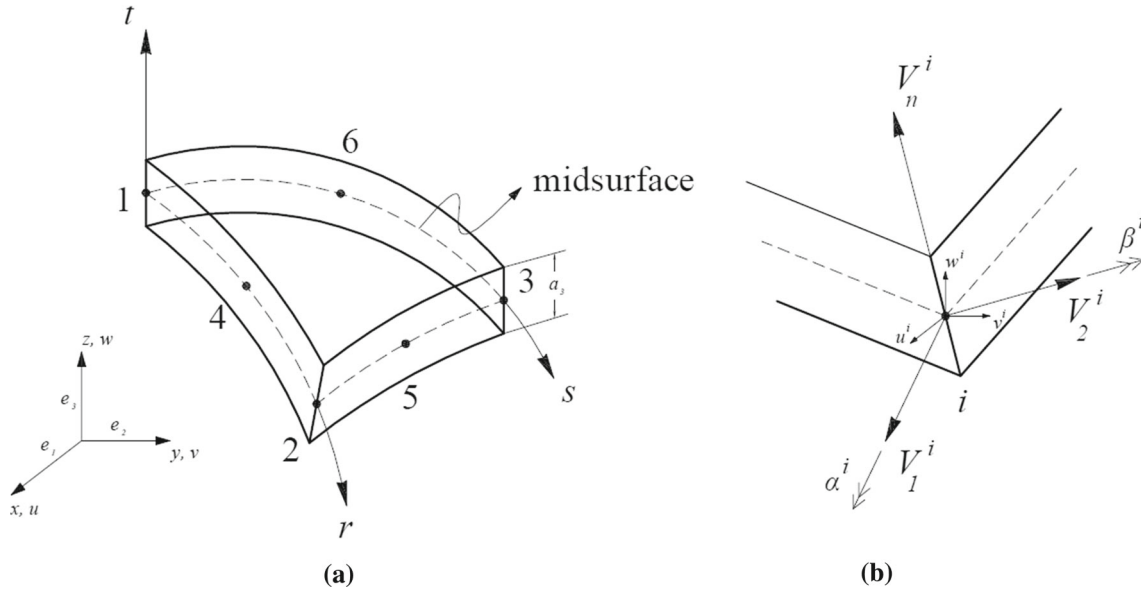


Fig. 1 Six-node triangular shell element: **a** Geometry of the element. **b** Definition of rotational degrees of freedom α_i and β_i

In this relation, two-dimensional interpolation functions of the six-node iso-parametric element are defined as $h_i(r, s)$. Moreover, the position vector of node i at the global Cartesian coordinate system is shown by ${}^t\vec{x}_i$. In addition, a_i and \vec{V}_n^i define the thickness and director vector of node i , respectively. The following equation defines the incremental displacement in the element configuration at time t to $t + \Delta t$:

$$\begin{aligned}\vec{u}(r, s, t) &= {}^{t+\Delta t}\vec{x}(r, s, t) - {}^t\vec{x}(r, s, t), \\ \vec{u}(r, s, t) &= \sum_{i=1}^6 h_i(r, s) \vec{u}_i + \frac{t}{2} \sum_{i=1}^6 a_i h_i \left({}^{t+\Delta t}\vec{V}_n^i - {}^t\vec{V}_n^i \right)\end{aligned}\quad (2)$$

where u_i is the incremental displacement at node i . Using the rotation matrix ${}^{t+\Delta t}Q^i$, the incremental director vector can be obtained as:

$${}^{t+\Delta t}\vec{V}_j^i = {}^{t+\Delta t}Q^{it} \vec{V}_j^i \quad (j = 1, 2, n). \quad (3)$$

The finite rotation tensor can be expanded using Taylor series expansion. Keeping the terms up to quadratic order and utilizing a consistent linearization [12], one can reach the following equation [19]:

$${}^{t+\Delta t}\vec{V}_n^i - {}^t\vec{V}_n^i = -\alpha_i {}^t\vec{V}_2^i + \beta_i {}^t\vec{V}_1^i - \frac{1}{2} (\alpha_i^2 + \beta_i^2) {}^t\vec{V}_n^i. \quad (4)$$

Here α_i and β_i are the rotations about the vectors ${}^tV_1^i$ and ${}^tV_2^i$. To determine the orientation of the director vector at time $t + \Delta t$ from time t , two unit vectors ${}^tV_1^i$ and ${}^tV_2^i$ are defined as follows:

$$\begin{aligned}{}^t\vec{V}_1^i &= \frac{e_2 \times {}^t\vec{V}_n^i}{|e_2 \times {}^t\vec{V}_n^i|}, \\ {}^t\vec{V}_2^i &= {}^t\vec{V}_n^i \times {}^t\vec{V}_1^i.\end{aligned}\quad (5)$$

Using Eqs. (2) and (4), the following incremental displacement can be established:

$$\vec{u}(r, s, t) = \sum_{i=1}^6 h_i(r, s) \vec{u}_i + \frac{t}{2} \sum_{i=1}^6 a_i h_i \left(-\alpha_i {}^t\vec{V}_2^i + \beta_i {}^t\vec{V}_1^i \right) - \frac{t}{4} \sum_{i=1}^6 a_i h_i \left[(\alpha_i^2 + \beta_i^2) {}^t\vec{V}_n^i \right]. \quad (6)$$

The incremental displacement can be divided into two parts, which are defined as linear part, u_l , and quadratic part, u_q . These are written in the subsequent form:

$$\begin{aligned}\bar{u}(r, s, t) &= \bar{u}_l(r, s, t) + \bar{u}_q(r, s, t), \\ \bar{u}_l(r, s, t) &= \sum_{i=1}^6 h_i(r, s) \bar{u}_i + \frac{t}{2} \sum_{i=1}^6 a_i h_i \left(-\alpha_i^t \bar{V}_2^i + \beta_i^t \bar{V}_1^i \right), \\ \bar{u}_q(r, s, t) &= -\frac{t}{4} \sum_{i=1}^6 a_i h_i \left[(\alpha_i^2 + \beta_i^2)^t \bar{V}_n^i \right].\end{aligned}\quad (7)$$

According to the kinematic Eq. (6), it is obvious that five degrees of freedom are considered at each node of the shell element.

3 Strain field

The covariant base vector of an element in the convected coordinate system, r_i , ($r_1 = r, r_2 = s, r_3 = t$), is obtained in the next form:

$$\begin{aligned}{}^0\bar{g}_i &= \frac{\partial^0 \bar{x}}{\partial r_i}, \\ {}^t\bar{g}_i &= \frac{\partial^t \bar{x}}{\partial r_i} = \frac{\partial^0 \bar{x}}{\partial r_i} + \frac{\partial^t \bar{u}}{\partial r_i} = {}^0\bar{g}_i + {}^t\bar{u}_{,i},\end{aligned}\quad (8)$$

In addition, covariant strain tensor, at time t with respect to time 0, has the following shape:

$${}^t_0\varepsilon_{ij} = \frac{1}{2} ({}^t\bar{g}_i \cdot {}^t\bar{g}_j - {}^0\bar{g}_i \cdot {}^0\bar{g}_j). \quad (9)$$

Therefore, the subsequent incremental covariant strains can be found:

$$\begin{aligned}{}^0\varepsilon_{ij} &= {}^{t+\Delta t}{}_0\varepsilon_{ij} - {}^t_0\varepsilon_{ij}, \\ {}^0\varepsilon_{ij} &= \frac{1}{2} (\bar{u}_{,i} \cdot {}^t\bar{g}_j + {}^t\bar{g}_i \cdot \bar{u}_{,j} + \bar{u}_{,i} \cdot \bar{u}_{,j}).\end{aligned}\quad (10)$$

The last relation has two linear and nonlinear parts. They are expressed as:

$$\begin{aligned}{}^0e_{ij} &= \frac{1}{2} \left(\frac{\partial \bar{u}_l}{\partial r_i} \cdot {}^t\bar{g}_j + {}^t\bar{g}_i \cdot \frac{\partial \bar{u}_l}{\partial r_j} \right) = B_{ij} \bar{U}, \\ {}^0\eta_{ij} &= \frac{1}{2} \left(\frac{\partial \bar{u}_l}{\partial r_i} \cdot \frac{\partial \bar{u}_l}{\partial r_j} \right) + \frac{1}{2} \left(\frac{\partial \bar{u}_q}{\partial r_i} \cdot {}^t\bar{g}_j + {}^t\bar{g}_i \cdot \frac{\partial \bar{u}_q}{\partial r_j} \right) = \frac{1}{2} \bar{U}^T N_{ij} \bar{U}\end{aligned}\quad (11)$$

where B_{ij} and N_{ij} denote the strain–displacement matrices. Furthermore, the nodal incremental displacement vector is defined by \bar{U} . In order to determine the components of the assumed covariant strain, the following transmission is employed for covariant strain components to improve the six-node triangular shell element:

$$\varepsilon_{ij}^{AS}(r, s, t) = \sum_{k=1}^n h_{ij}^k(r, s) \hat{\varepsilon}_{ij} \Big|_{(r_{ij}^k, s_{ij}^k, t)}. \quad (12)$$

In this equation, the next corresponding variables are utilized:

$$\begin{aligned}h_{ij}^k(r_{ij}^l, s_{ij}^l) &= \delta_{kl}, \\ \hat{\varepsilon}_{ij} &= \varepsilon_{kl} (\bar{g}^k \cdot \hat{g}_i) (\bar{g}^l \cdot \hat{g}_j), \\ \hat{g}_i(r, s, t) &= \bar{g}_i(1/3, 1/3, t), \\ \bar{g}^i &= g^{ij} g_j, \\ g^{ij} &= \frac{D^{ij}}{|J|^2}\end{aligned}\quad (13)$$

where \vec{g}^l denote the contra-variant base vector of the element. Note that δ_{kl} and D^{ij} are Kronecker delta and cofactor of the metric tensor, respectively. The following interpolation functions are used for in-plane strains in the convected coordinates:

$$\begin{aligned}\hat{\varepsilon}_{rr} &= a_1 + b_1 r + c_1 s, \\ \hat{\varepsilon}_{ss} &= a_2 + b_2 r + c_2 s, \\ \hat{\varepsilon}_{qq} &= a_3 + b_3 r + c_3 (1 - r - s).\end{aligned}\quad (14)$$

In these equalities, the following parameters are employed:

$$\begin{aligned}a_1 &= m_{rr}^{(1)} - l_{rr}^{(1)}, \quad b_1 = 2l_{rr}^{(1)}, \quad c_1 = \sqrt{3} \left(\hat{\varepsilon}_{crr}^{(1)} - a_1 - b_1 r_1 \right), \\ a_2 &= m_{ss}^{(2)} - l_{ss}^{(2)}, \quad b_2 = \sqrt{3} \left(\hat{\varepsilon}_{css}^{(2)} - a_2 - c_2 s_1 \right), \quad c_2 = 2l_{ss}^{(2)}, \\ a_3 &= m_{qq}^{(3)} - l_{qq}^{(3)}, \quad b_3 = -2l_{qq}^{(3)}, \quad c_3 = \sqrt{3} \left(\hat{\varepsilon}_{cqq}^{(3)} - a_3 - b_3 r_1 \right), \\ m_{jj}^{(i)} &= \frac{1}{2} \left(\hat{\varepsilon}_{1jj}^{(i)} + \hat{\varepsilon}_{2jj}^{(i)} \right), \quad l_{jj}^{(i)} = \frac{\sqrt{3}}{2} \left(\hat{\varepsilon}_{2jj}^{(i)} - \hat{\varepsilon}_{1jj}^{(i)} \right): \quad j = r, s, q \quad i = 1, 2, 3.\end{aligned}\quad (15)$$

For transverse shear strains, the subsequent interpolation functions are used:

$$\begin{aligned}\hat{\varepsilon}_{rt} &= a_1 + b_1 r + c_1 s + d_1 r s + f_1 s^2, \\ \hat{\varepsilon}_{st} &= a_2 + b_2 r + c_2 s + d_2 r s + f_2 r^2\end{aligned}\quad (16)$$

where the following coefficients are defined:

$$\begin{aligned}a_1 &= m_{rt}^{(1)} - l_{rt}^{(1)}, \quad b_1 = 2l_{rt}^{(1)}, \quad c_1 = 6\hat{\varepsilon}_{crt} - 3\hat{\varepsilon}_{cst} + 2m_{st}^{(3)} - 2m_{rt}^{(3)} - 4a_1 - b_1 + a_2, \\ a_2 &= m_{st}^{(2)} - l_{st}^{(2)}, \quad b_2 = -3\hat{\varepsilon}_{crt} + 6\hat{\varepsilon}_{cst} - 2m_{st}^{(3)} + 2m_{rt}^{(3)} + a_1 - 4a_2 - c_2, \quad c_2 = 2l_{st}^{(2)}, \\ f_1 &= -6\hat{\varepsilon}_{crt} + 3\hat{\varepsilon}_{cst} - 3m_{st}^{(3)} - l_{st}^{(3)} + 3m_{rt}^{(3)} + l_{rt}^{(3)} + 3a_1 + b_1 + c_2, \\ f_2 &= 3\hat{\varepsilon}_{crt} - 6\hat{\varepsilon}_{cst} + 3m_{st}^{(3)} - l_{st}^{(3)} - 3m_{rt}^{(3)} + l_{rt}^{(3)} + b_1 + 3a_2 + c_2, \\ d_1 &= -f_2, \quad d_2 = -f_1, \\ m_{jt}^{(i)} &= \frac{1}{2} \left(\hat{\varepsilon}_{1jt}^{(i)} + \hat{\varepsilon}_{2jt}^{(i)} \right), \quad l_{jt}^{(i)} = \frac{\sqrt{3}}{2} \left(\hat{\varepsilon}_{2jt}^{(i)} - \hat{\varepsilon}_{1jt}^{(i)} \right): \quad j = r, s \quad i = 1, 2, 3.\end{aligned}\quad (17)$$

Based on the last equations, the next interpolation function for in-plane shear strain is obtained:

$$\hat{\varepsilon}_{rs} = \frac{1}{2} \left(\hat{\varepsilon}_{rr} + \hat{\varepsilon}_{ss} \right) - \hat{\varepsilon}_{qq}.\quad (18)$$

It should be noted that the membrane locking test of this element was considered by Kim and Bathe [26]. On the other hand, to alleviate the shear locking, the interpolation of strain is applied in some tying points. The positions of tying points are depicted in Figs. 2 and 3. It should be added that these positions are given by [23]:

$$\begin{aligned}r_1 &= s_1 = \frac{1}{2} - \frac{1}{2\sqrt{3}}, \\ r_2 &= s_2 = \frac{1}{2} + \frac{1}{2\sqrt{3}}, \\ r_3 &= s_3 = \frac{1}{3}, \\ r_c &= s_c = \frac{1}{\sqrt{3}}.\end{aligned}\quad (19)$$

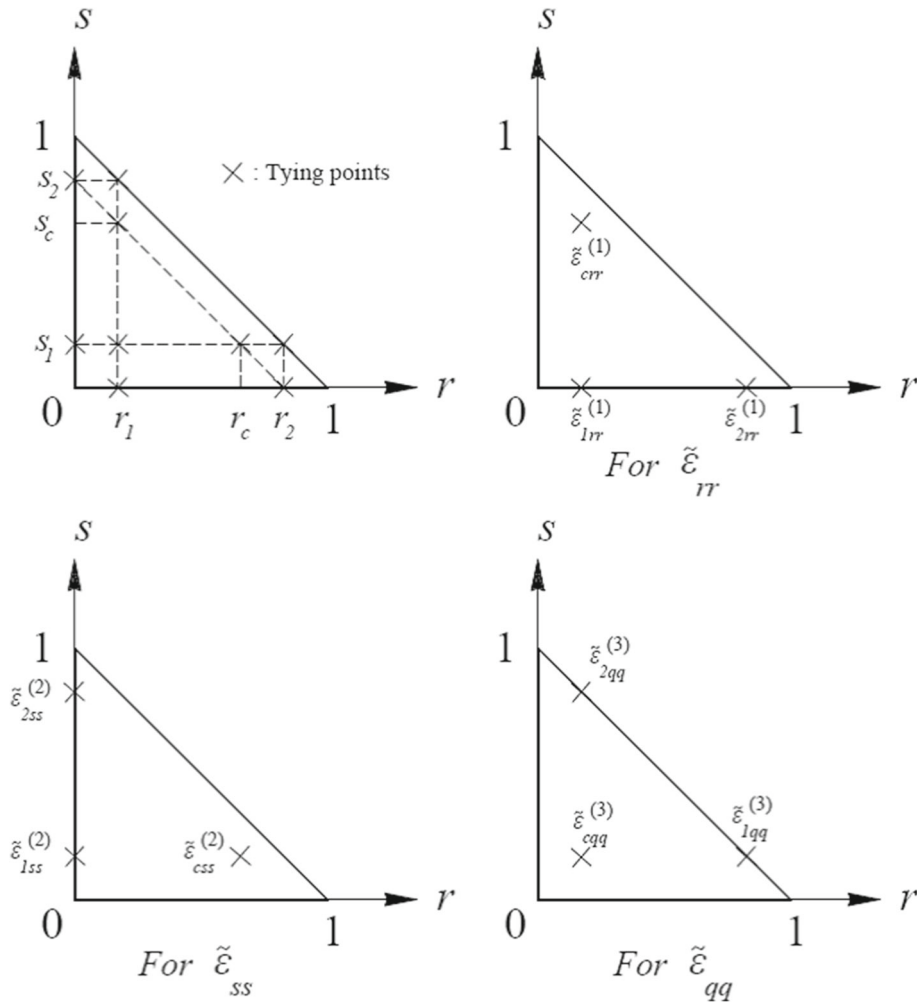


Fig. 2 In-plane strain tying positions for the shell element with linear normal strain along edges

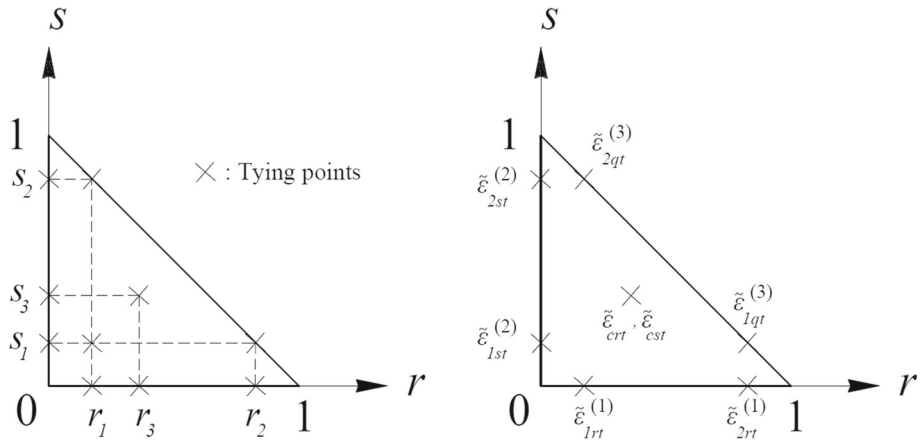


Fig. 3 Tying points for the transverse shear strain interpolation of the shell element

4 Finite element procedure

The element stiffness matrix can be established either in the convected or in the global coordinates system. In this paper, all the relations are transferred to a global coordinates system in which the covariant base vectors are utilized. To achieve the governing equations of the shell element, the principle of virtual work and total Lagrangian formulation is employed. The following equation denotes the linearization incremental relation:

$$\int_{0V} {}_0\tilde{C}^{ijkl} {}_0\tilde{e}_{kl} \delta_0 \tilde{e}_{ij}^0 dV + \int_{0V} {}_0^t \tilde{S}^{ij} \delta_0 \tilde{\eta}_{ij}^0 dV = {}^{t+\Delta t} \mathfrak{R} - \int_{0V} {}_0^t \tilde{S}^{ij} \delta_0 \tilde{e}_{ij}^0 dV \quad (20)$$

where ${}_0^t \tilde{S}^{ij}$ represents the contra-variant components of the second Piola-Kirchhoff stress tensor. Moreover, the linear and nonlinear covariant components of the Green–Lagrange strain tensor are denoted by ${}_0\tilde{e}_{ij}$ and ${}_0\tilde{\eta}_{ij}$, respectively. By substituting the incremental stress–strain relations in the governing equation, the linear and nonlinear stiffness matrix in the incremental equilibrium equation can be obtained as follows:

$$({}_0^t K_L + {}_0^t K_{NL}) \vec{q} = {}^{t+\Delta t} \mathfrak{R} - {}_0^t F. \quad (21)$$

In the last relation, \vec{q} is the vector of nodal displacements.

5 Computer programming

Based on the proposed formulation, a computer program was developed by the authors. Both generalized displacement control method (GDCM) and Newton–Raphson (NR) are utilized in this code. Verification studies are carried out by solving several benchmark problems. A brief explanation of the GDCM steps is given in the following:

Step 1 Specify the initial load factor step ($\delta\lambda_0$), global displacement $\{\mathbf{u}_P\} = 0$ and $\{\mathbf{u}_R\} = 0$, unbalanced load vector $\{\mathbf{R}\}_0 = 0$, and compute the global external load vector $\{\mathbf{P}\}$.

Step 2 Initialize analysis step $i = 0$

Step 3 Calculate the initial director vectors of each node ($\{\mathbf{V}_n\}_0, \{\mathbf{V}_1\}_0, \{\mathbf{V}_2\}_0$)

Step 4 Initialize iteration $j = 0$

Step 5 Increment $j = j + 1$

Step 6 Find the global stiffness matrix $[\mathbf{K}_j^i] = [\mathbf{K}_j^i]_L + [\mathbf{K}_j^i]_{NL}$ using Eqs. (19) and (20).

Step 7 Compute the vector of displacement $\{\delta\mathbf{u}_P\}_j^i$ according to

$$\{\delta\mathbf{u}_P\}_j^i \leftarrow [\mathbf{K}]_{j-1}^{i-1} \{\bar{\mathbf{P}}\},$$

Step 8 Calculate $\{\delta\mathbf{u}_R\}_j^i$ based on the $\{\delta\mathbf{u}_R\}_j^i \leftarrow [\mathbf{K}]_{j-1}^{i-1} \{\mathbf{R}\}_{j-1}^i$.

Step 9 Compute $\delta\lambda_j^i$ according to the following procedure:

$$\delta\lambda_j^i = \begin{cases} \frac{c}{\delta\lambda_1^i \{\delta\mathbf{u}_P\}_1^{i-1T} \{\delta\mathbf{u}_P\}_1^i} & \text{for } j = 1 \\ -\frac{\{\delta\mathbf{u}_P\}_1^{i-1T} \{\delta\mathbf{u}_R\}_j^i}{\{\delta\mathbf{u}_P\}_1^{i-1T} \{\delta\mathbf{u}_P\}_j^i} & \text{for } j \geq 2 \end{cases} \quad (22)$$

where c is obtained by letting $\{\delta\mathbf{u}_P\}_1^1 = \{\delta\mathbf{u}_P\}_1^0$, which leads to the following result:

$$c = (\delta\lambda_1^1)^2 \left(\{\delta\mathbf{u}_P\}_1^{1T} \cdot \{\delta\mathbf{u}_P\}_1^1 \right), \quad (23)$$

Furthermore, the load factor step for the first iteration of each step is obtained based on the initial value of ($\delta\lambda_0$) such as below:

$$\delta\lambda_1^i = \pm(\delta\lambda_0) \sqrt{\frac{\{\delta\mathbf{u}_P\}_1^{iT} \{\delta\mathbf{u}_P\}_1^i}{\{\delta\mathbf{u}_P\}_1^{i-1T} \{\delta\mathbf{u}_P\}_1^i}}. \quad (24)$$

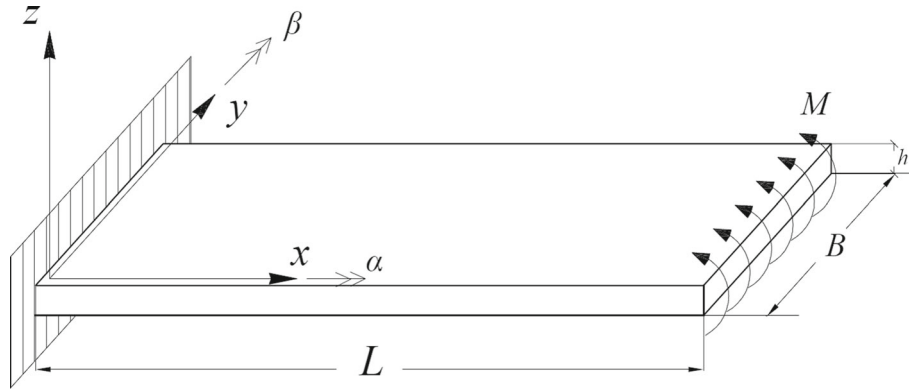


Fig. 4 Cantilever bending plate under the end distributed moment

Step 10 Update the total load factor based on $\lambda^i \leftarrow \lambda^i + \delta\lambda_j^i$.

Step 11 Update the external load vector using $\{\mathbf{P}\}^i \leftarrow \{\mathbf{P}\}^i + \delta\lambda_j^i \{\bar{\mathbf{P}}\}$.

Step 12 Update the displacement vector according to

$$\{\mathbf{u}\}^i \leftarrow \{\mathbf{u}\}^i + \delta\lambda_j^i \{\delta\mathbf{u}_P\}_j^i + \{\delta\mathbf{u}_R\}_j^i.$$

Step 13 Calculate the internal force vector $\{\mathbf{P}_{\text{int}}\}^i$ employing Eq. (19).

Step 14 Compute the unbalanced load vector based on $\{\mathbf{R}\}_j^i \leftarrow \{\mathbf{P}\}^i - \{\mathbf{P}_{\text{int}}\}^i$.

Step 15 If the convergence is achieved, then go to the next step $i \leftarrow i + 1$, otherwise go to step 5. The convergence criterion is defined as follows:

$$\frac{\|\mathbf{R}_j^i\|}{\|\bar{\mathbf{P}}\|} < \text{tolerance}. \quad (25)$$

It should be added that in this step the maximum number of iterations is controlled. If the number of iterations (j) exceeds 10, the procedure returns to step 9 and the value of the load factor increment is decreased.

Note that in order to get the global stiffness matrix and calculate the related integrals in Eq. (19), seven Gaussian points in the $r - s$ plane have been utilized. Figure 18 in the ‘‘Appendix’’ illustrates the flowchart of the authors’ program.

6 Numerical study

To evaluate the performance of the six-node triangular element in large deformation and rotation problems, several popular benchmark structural shells are treated. The results of these geometric nonlinear analyses are reported and compared to the near-exact solutions, which can be found in the literature [1,29,47,48]. Hereby, the high accuracy of the new element is established.

6.1 Cantilever plate subjected to end moment

A cantilever bending plate subjected to end distributed moment is illustrated in Fig. 4. In this example, the ability of the six-node triangular element will be compared with the MITC3+ element for large deformation analysis. This shell element was investigated by Jeon et al. [29]. The geometry characteristics of this structure and its material properties are given in Table 1. The exact solution of this problem is available based on the classical bending formula.

To obtain the results, 32 elements are used for finite element discretization. The distributed bending moment is gradually increased up to $2\pi M_0$ with $M_0 = EI/L$. Note that $2\pi M_0$ equals the maximum value of the applied load. It is worth mentioning that 32 MITC3+ elements were used to find the solution for this problem by Jeon et al. [29]. Numerical findings clearly demonstrate the high accuracy of the authors’ element for

Table 1 Geometry and material characteristics of plate under bending moment

E	ν	L	B	H
1.2×10^6	0.00	12.00	1.0	0.1

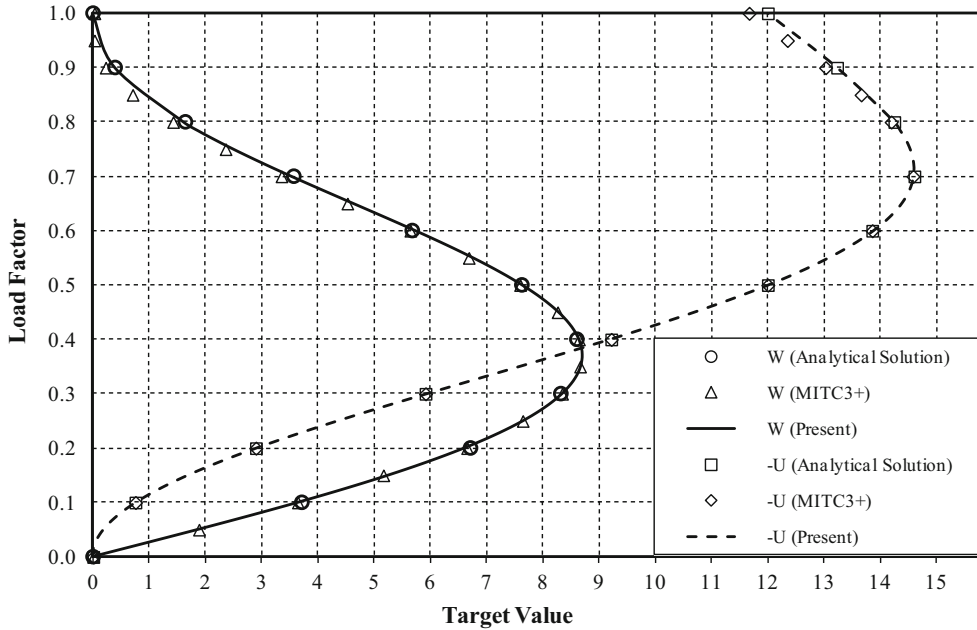


Fig. 5 Load–displacement curves of cantilever plate under the end distributed moment

nonlinear analysis. The present study is in excellent correspondence with the exact solution. Figure 5 displays the variation of displacement versus load steps. The analytical solution, six-node element and MITC3+ are depicted in Fig. 5. For this problem, the exact or analytical solution is found from classic formula $\frac{1}{\rho} = \frac{M}{EI}$. In fact, the tip deflection of the cantilever plate, U or W , is obtained as follows:

$$\begin{aligned} \frac{U}{L} &= \frac{M_0}{M} \sin\left(\frac{M}{M_0}\right) - 1, \\ \frac{W}{L} &= \frac{M_0}{M} \left(1 - \cos\left(\frac{M}{M_0}\right)\right). \end{aligned} \tag{26}$$

6.2 Cantilever plate subjected to axial force

In this example, the buckling and post-buckling behaviors of the cantilever plate are studied. The plate subjected to compressive axial load is shown in Fig. 6. It is aimed to find the capability of the six-node element to deal with pre-buckling and post-buckling of shell structures. The material and geometry of the structure are listed in Table 2. To achieve appropriate responses, 32 elements are used.

A small perturbation should be considered in the system to achieve the post-buckling equilibrium path. The maximum distributed axial compressive load is assumed to be 7000. Furthermore, the compressive load should be applied with an imperfection angle of 1/1000 to obtain the secondary path. Therefore, there is a small out-of-plane loading that causes the post-buckling of the plate beside the in-plane compressive load.

The obtained results are compared with the solutions reported by Arciniega and Reddy [1]. In addition, the exact solution of the critical load was obtained by Euler’s formula ($P_{cr} = 1124.2096$). Figure 7 shows the deformation responses of the present study and the exact solution. It is observed that the present results are in good agreement with the responses reported by Arciniega and Reddy.

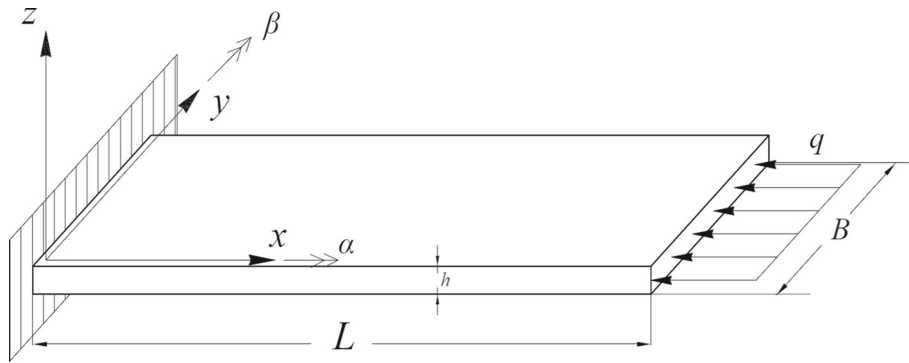


Fig. 6 Cantilever plate subjected to axial compressive load

Table 2 Geometry and material characteristics of axially loaded cantilever plate

E	ν	L	B	H
2.0×10^{11}	0.30	0.50	0.075	0.0045

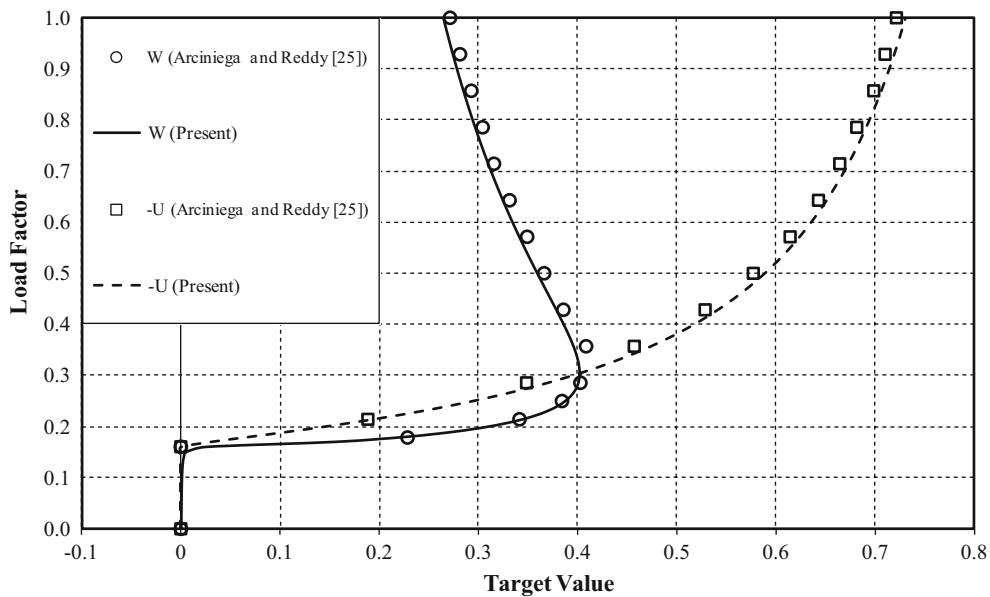


Fig. 7 Load–displacement curves of cantilever plate subjected to axial compressive load

Table 3 Geometry and material characteristics of the slit annular plate

E	ν	R_i	R_e	h
21×10^6	0.00	6.00	10.00	0.03

6.3 Slit annular plate under end shear force

A slit annular clamped plate subjected to end transverse shear force is analyzed in this part. The material and geometric properties of the plate are given in Table 3. The number of elements used to achieve the appropriate result is 300. On the other hand, the number of MITC3+ elements employed to obtain agreeable results was equal to 360 [29]. Figure 8 illustrates the slit annular plate which is subjected to the end distributed transverse shear force.

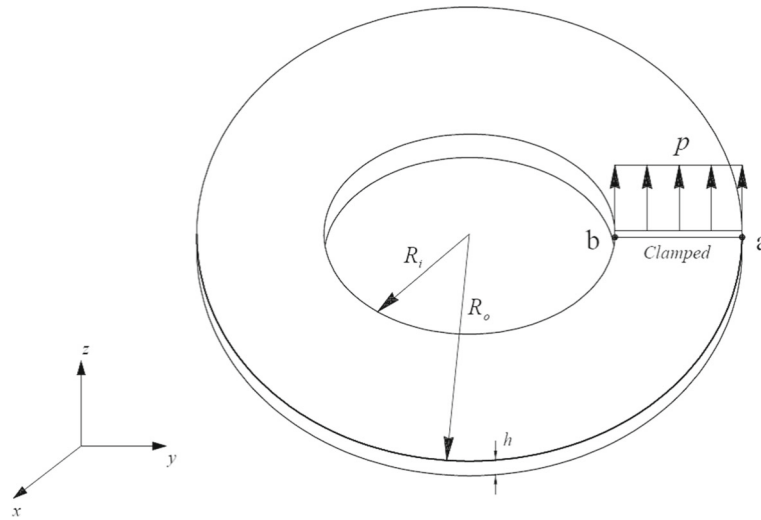


Fig. 8 Slit annular plate under end shear force

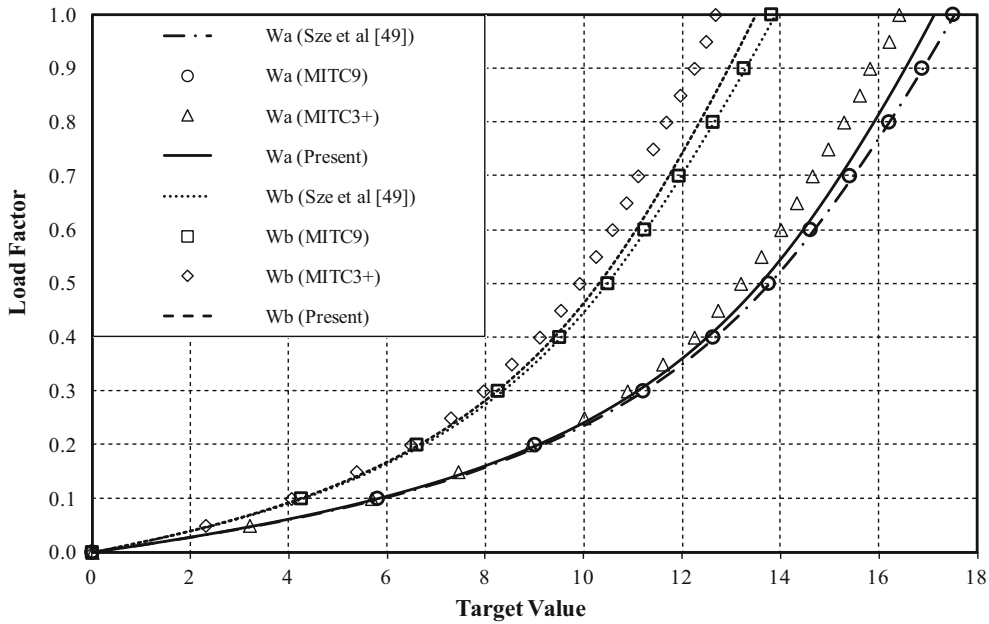


Fig. 9 Load–displacement curves of slit annular plate under end shear force

The distributed transverse shear force, with $p_{max} = 3.2$, is applied incrementally at one end of the plate. The other end of the plate is fully clamped. Figure 9 shows the deformation responses of the present study with near-exact solution [29]. In this Figure, it is concluded that in spite of using a smaller number of elements the accuracy of the authors' element is higher than that of MITC3+.

It should be mentioned that the load factor is chosen by the researcher only for the first step and updated automatically. Thus, based on the algorithm of GDCM, the number of iterations and convergence rate is obtained for the first step of loading. The results are reported in Table 4.

6.4 Hemispherical shell subjected to alternating radial forces

In this problem, a full pinched hemispherical shell is considered, which is shown in Fig. 10. This shell is subjected to two inward and two outward forces. Here, a hole is assumed at the top of the shell. This structure

Table 4 Convergence of residual within equilibrium for slit annular plate

Load increment	No. of iteration	Tolerance
0.005	5	$10^2 10^{-1} 10^{-2} 10^{-5} 10^{-7}$
0.010	7	$10^3 10^0 10^{-1} 10^{-2} 10^{-3} 10^{-4} 10^{-6}$
0.015	8	$10^3 10^2 10^1 10^0 10^{-1} 10^{-2} 10^{-3} 10^{-6}$
0.020	13	$10^4 10^1 10^2 10^1 10^1 10^0 10^0 10^0 10^0 10^{-2} 10^{-2} 10^{-5} 10^{-6}$
0.025	17	$10^4 10^2 10^2 10^2 10^1 10^1 10^1 10^0 10^0 10^0 10^0 10^{-1} 10^{-1} 10^{-2} 10^{-3} 10^{-5} 10^{-7}$
0.030	13	$10^4 10^3 10^1 10^2 10^0 10^1 10^1 10^1 10^1 10^0 10^{-3} 10^{-2} 10^{-6}$
0.035	21	$10^4 10^3 10^2 10^3 10^1 10^3 10^1 10^2 10^1 10^1 10^1 10^1 10^1 10^1 10^0 10^0 10^0$ $10^{-1} 10^{-2} 10^{-4} 10^{-6}$
0.040	No convergence	

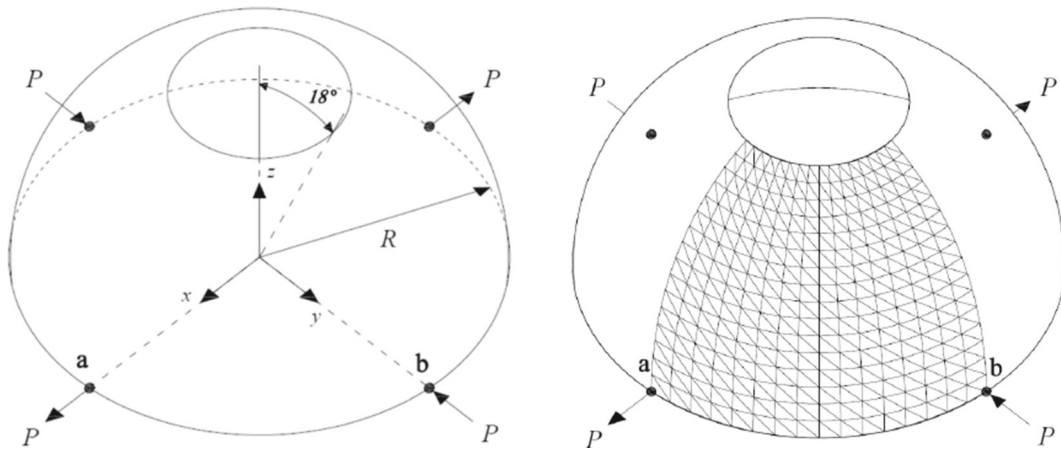


Fig. 10 Hemispherical shell subjected to alternating radial forces

Table 5 Geometry and material characteristics of hemispherical shell

E	ν	R
6.825×10^7	0.30	10.00

is analyzed considering three thicknesses of 0.4, 0.04, and 0.004. The material and geometric properties of the shell are found in Table 5.

Due to symmetry, a quarter of the shell will be analyzed. In this case, the number of elements is equal to 512. To validate the results with other references, the thickness of 0.04 is chosen for the structure at first. In this case, the maximum load is assumed to be $P_{max} = 400$. The results of radial displacements of points (a) and (b) are reported in Fig. 11. Furthermore, these are compared with the results obtained from MITC3+ and the near-exact solutions [29,48]. The same mesh is used for MITC3+ discretization. Since the order of the present element is higher than that of MITC3+, higher accuracy is expected to be achieved. The obtained results confirm this prediction. Moreover, two other analyses of a hemispherical shell with thickness of 0.4 and 0.004 are performed to show the ability of the new element in the nonlinear analysis of very thin to moderately thick shells. The results are depicted in Fig. 12. In these cases, the maximum load is equal to 400,000 and 0.4, respectively.

A convergence study was performed to show the accuracy and capability of the proposed shell element in the geometrically nonlinear analysis. Hence, five types of mesh discretization are considered, including $(4 \times 4) \times 2$, $(8 \times 8) \times 2$, $(12 \times 12) \times 2$, $(16 \times 16) \times 2$ and $(20 \times 20) \times 2$. The results are compared with those reported in [47] and depicted in Fig. 13. The relation for the error ratio is given by $|U_a - U^*|/U^*$. It should be added that the value of U^* is assumed to be 4.07429. Moreover, the convergences of displacements for points (a) and (b) are reported for the different numbers of elements and degrees of freedom in Table 6.

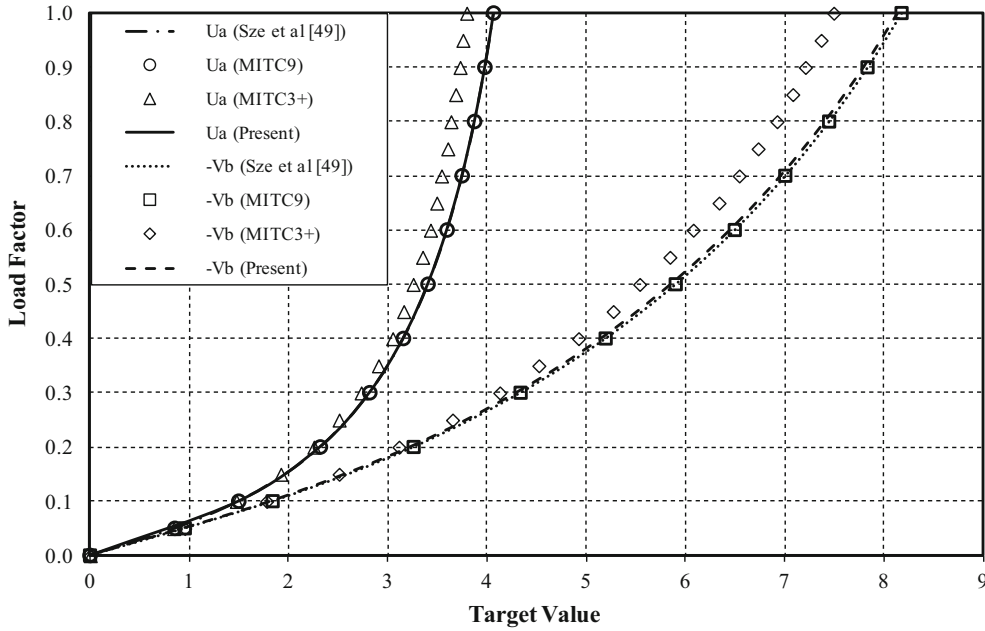


Fig. 11 Load–displacement curves of a hemispherical shell with thickness of 0.04

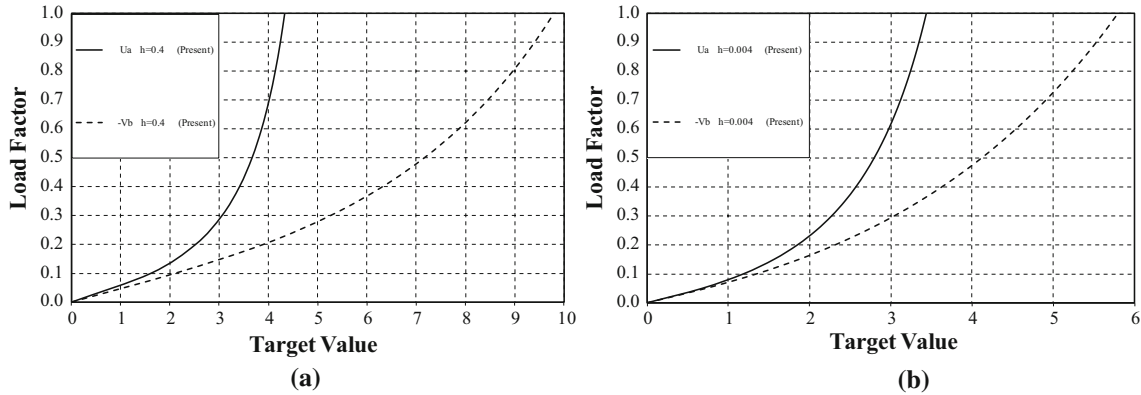


Fig. 12 Load–displacement curves of a hemispherical shell, **a** $h = 0.4$, **b** $h = 0.004$

6.5 Clamped semicylindrical shell subjected to point load

Another popular benchmark problem is a semicylindrical shell shown in Fig. 14. One end of this structure is clamped, while the other side is free. Moreover, two sides of the semicylindrical shell are pinned. This structure is subjected to a point load at the free end. The geometry and properties of the material used in this problem are reported in Table 7.

The maximum load which is applied at the end of the shell is $P_{max} = 2000$. In this example, one half of the structure is modeled due to symmetry. To achieve high accuracy, the number of elements used for this problem is considered to be 400. In addition, deflection results at the point (a) are demonstrated in Fig. 15. These results are compared with the near-exact solution, and those obtained by MITC3+ element for the same regular mesh [29]. As it is depicted in Fig. 15, the accuracy of the authors’ results is better than the responses of MITC3+.

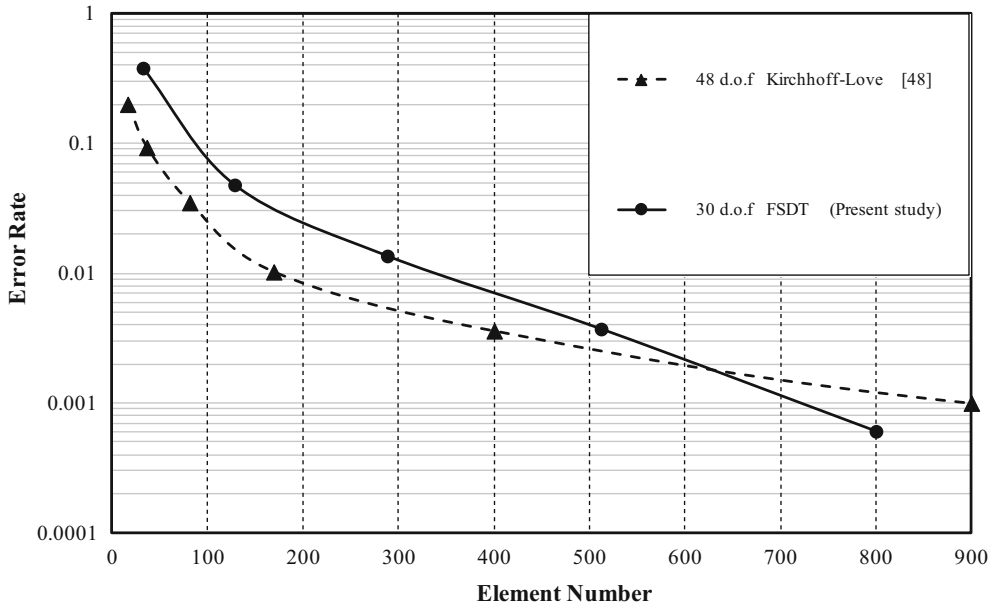


Fig. 13 Mesh convergence rate of a hemispherical shell for displacement of U_a

Table 6 Convergence of displacements for different numbers of elements/degree of freedom

Element	D.O.F	U_a	$-V_b$
32	405	2.5248	3.0001
128	1445	3.8790	7.5037
288	3125	4.0189	7.9998
512	5445	4.0591	8.1325
800	8405	4.0718	8.1685

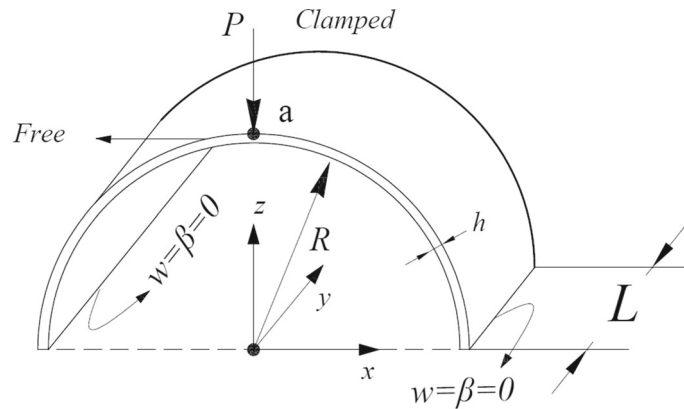


Fig. 14 Clamped semicylindrical shell subjected to point load at the free edge

Table 7 Geometry and material characteristics of clamped semicylindrical shell

E	ν	R	L	h
2.0685×10^7	0.30	1.06	0.3048	0.03

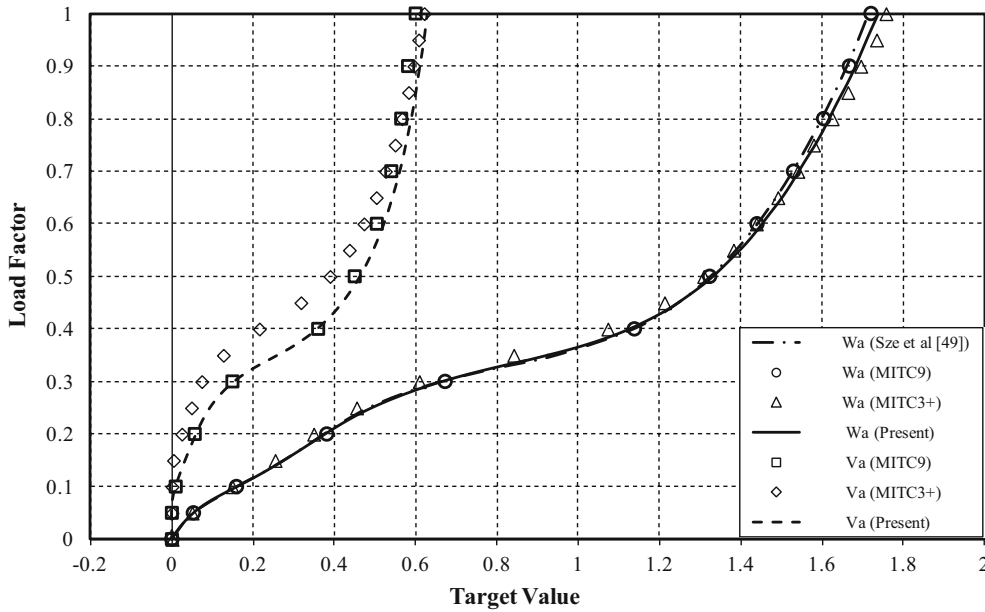


Fig. 15 Load–displacement curves of clamped semicylindrical shell subjected to point load

Table 8 Geometry and material characteristics of open-ended cylindrical shell

E	ν	R	L	H
10.50×10^6	0.3125	4.953	10.35	0.094

6.6 Pullout of an open-ended cylindrical shell

A cylindrical shell which is opened at two ends is subjected to two opposite tensile loads. Figure 16 shows the configuration of this problem. The geometric properties of this structure are found in Table 8. Besides, the maximum load applied at the middle of the shell is equal to $P_{max} = 40,000$.

The number of elements employed for this problem is assumed to be 200. Owing to symmetry, one-eighth of the shell is considered for the analysis. The results obtained from this analysis indicate the high accuracy of the new element. In addition, the comparison between the authors’ results and the solution obtained by Sze et al. [48] is illustrated in Fig. 17. Although the results obtained for the deflection of points (b) and (c) differ from the near-exact responses at the end of the equilibrium path, the answers of deflection at the location of the applied load coincide with the reference solution.

7 Conclusions

In this paper, a geometrically nonlinear formulation of a new shell element was developed. To avoid shear and membrane locking, an interpolation of strain fields for some special tying points was employed. Besides, the total Lagrangian formulation and Green strain functions were used to establish the nonlinear formulation. A computer program was developed by the authors. Moreover, various popular nonlinear benchmarks, including plate and shell structures, were solved using the proposed element. The obtained results were compared with the available responses presented by other researchers. According to the findings, superior efficiency and versatility of the authors’ shell element compared to MITC3+ were concluded. It should be mentioned that the presented element can be easily used in shell structures having curved side.

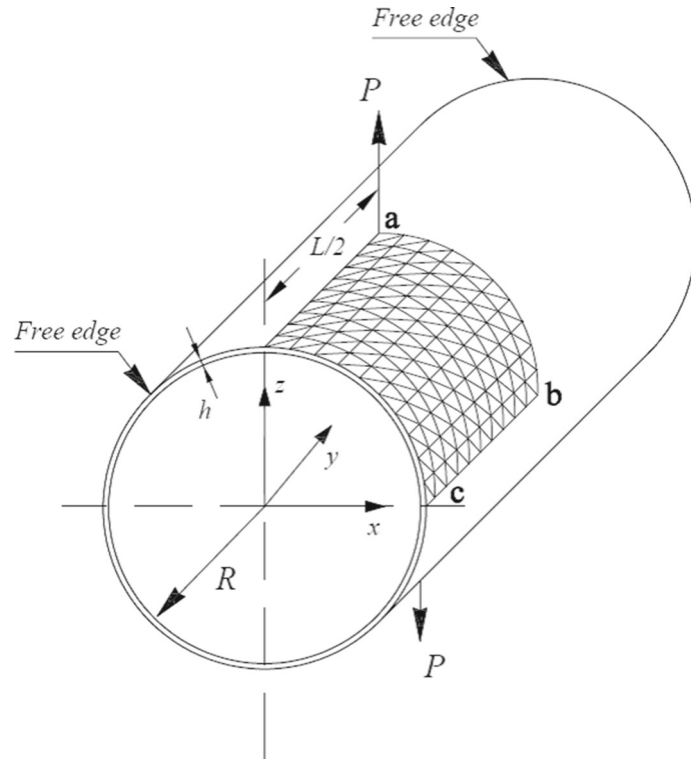


Fig. 16 Open-ended cylindrical shell

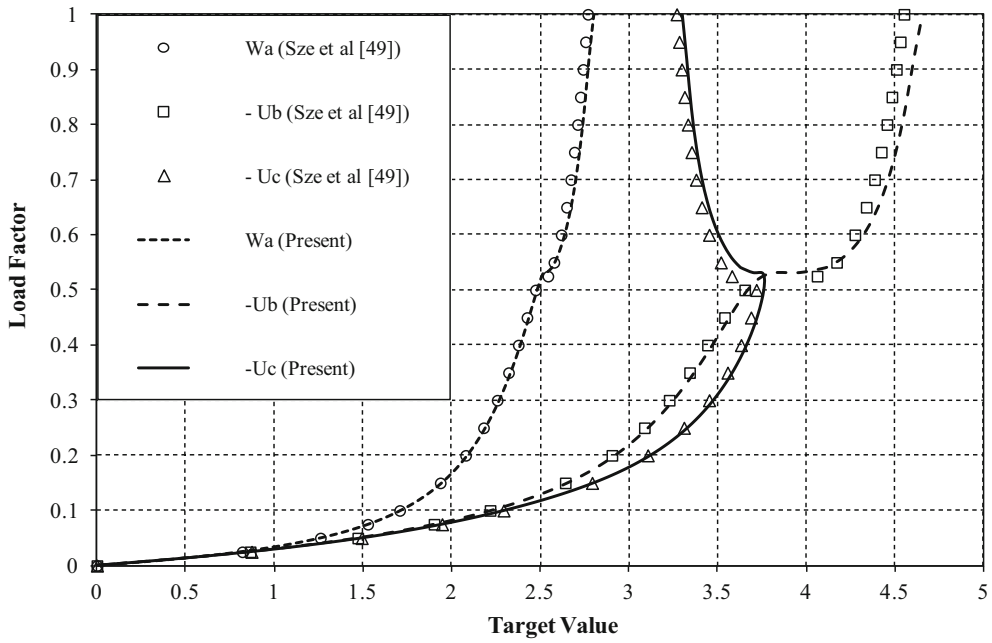


Fig. 17 Load-displacement curves of an open-ended cylindrical shell pulled out

Appendix

In Fig. 18, the flowchart is prepared to present a concise explanation of the geometrically nonlinear shell analysis procedure. It should be added that the following method is known as the generalized displacement control method (GDCM).

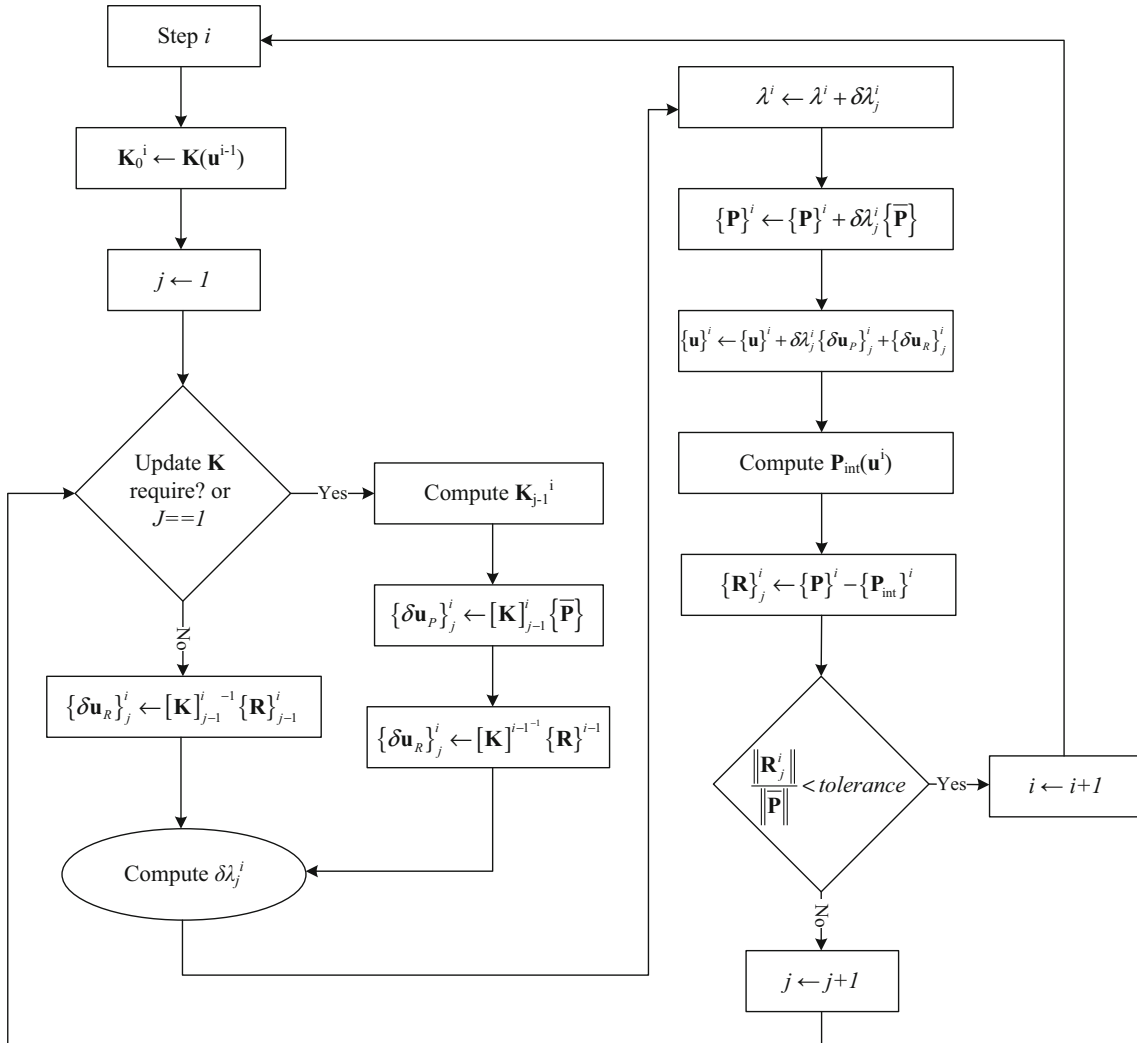


Fig. 18 Flowchart of nonlinear analysis procedure

References

1. Arciniega, R.A., Reddy, J.N.: Tensor-based finite element formulation for geometrically nonlinear analysis of shell structures. *Comput. Methods Appl. Mech. Eng.* **196**, 1048–1073 (2007)
2. Ahmad, S., Irons, B., Zienkiewicz, O.C.: Analysis of thick and thin shell structures by curved finite elements. *Int. J. Numer. Methods Eng.* **2**, 419–451 (1970)
3. Hughes, T.J.R., Liu, W.K.: Nonlinear finite element analysis of shells: Part I. Three-dimensional shells. *Comput. Methods Appl. Mech. Eng.* **26**, 331–362 (1981)
4. Hughes, T.J.R., Liu, W.K.: Nonlinear finite element analysis of shells-part II. Two-dimensional shells. *Comput. Methods Appl. Mech. Eng.* **27**, 167–181 (1981)
5. Hughes, T.J.R., Carnoy, E.: Nonlinear finite element shell formulation accounting for large membrane strains. *Comput. Methods Appl. Mech. Eng.* **39**, 69–82 (1983)

6. Dvorkin, E.N., Bathe, K.J.: A continuum mechanics based four-node shell element for general nonlinear analysis. *Eng. Comput.* **1**, 77–88 (1984)
7. Park, K.C., Stanley, G.M.: A curved C0 shell element based on assumed natural-coordinate strains. *J. Appl. Mech.* **53**, 278–290 (1986)
8. Liu, W.K., Law, E.S., Lam, D., Belytschko, T.: Resultant-stress degenerated-shell element. *Comput. Methods Appl. Mech. Eng.* **55**, 259–300 (1986)
9. Huang, H.C., Hinton, E.: A new nine node degenerated shell element with enhanced membrane and shear interpolation. *Int. J. Numer. Methods Eng.* **22**, 73–92 (1986)
10. Hsiao, K.M., Chen, Y.R.: Nonlinear analysis of shell structures by degenerated isoparametric shell element. *Comput. Struct.* **31**, 427–438 (1989)
11. Stanley, G.: *Continuum-Based Shell Elements*. Stanford University, Stanford (1985)
12. Bathe, K.J.: *Finite Element Procedures in Engineering Analysis*. Prentice-Hall, Englewood Cliffs (1982)
13. Crisfield, M.: *Finite Elements on Solution Procedures for Structural Analysis, (I) Linear Analysis*. Pineridge Press, Swansea (1986)
14. Simo, J.C., Fox, D.D.: On a stress resultant geometrically exact shell model. Part I: formulation and optimal parametrization. *Comput. Methods Appl. Mech. Eng.* **72**, 267–304 (1989)
15. Chapelle, D., Oliveira, D.L., Buclelem, M.L.: MITC elements for a classical shell model. *Comput. Struct.* **81**, 523–533 (2003)
16. Cho, M., Roh, H.Y.: Development of geometrically exact new shell elements based on general curvilinear co-ordinates. *Int. J. Numer. Methods Eng.* **56**, 81–115 (2003)
17. Chinosi, C., Della Croce, L., Scapolla, T.: Hierarchic finite elements for thin Naghdi shell model. *Int. J. Solids Struct.* **35**, 1863–1880 (1998)
18. Bathe, K.J., Dvorkin, E.N.: A formulation of general shell elements—the use of mixed interpolation of tensorial components. *Int. J. Numer. Methods Eng.* **22**, 697–722 (1986)
19. Dvorkin, E.N.: Nonlinear analysis of shells using the MITC formulation. *Arch. Comput. Methods Eng.* **2**, 1–50 (1995)
20. Dvorkin, E.N.: On nonlinear finite element analysis of shell structures. In: Bathe, K.J. (ed.) *Mechanical Engineering*. Massachusetts Institute of Technology, Cambridge (1984)
21. Lee, P.S.: On triangular finite elements for general shell structures. In: Bathe, K.J. (ed.) *Civil and Environmental Engineering*. Massachusetts Institute of Technology, Cambridge (2004)
22. Chapelle, D., Bathe, K.-J.: *The Finite Element Analysis of Shells—Fundamentals*. Springer, Berlin (2011)
23. Lee, P.S., Bathe, K.J.: Development of MITC isotropic triangular shell finite elements. *Comput. Struct.* **82**, 945–962 (2004)
24. Lee, P.S., Noh, H.C., Bathe, K.J.: Insight into 3-node triangular shell finite elements: the effects of element isotropy and mesh patterns. *Comput. Struct.* **85**, 404–418 (2007)
25. Lee, Y., Yoon, K., Lee, P.S.: Improving the MITC3 shell finite element by using the Hellinger-Reissner principle. *Comput. Struct.* **110–111**, 93–106 (2012)
26. Kim, D.N., Bathe, K.J.: A triangular six-node shell element. *Comput. Struct.* **87**, 1451–1460 (2009)
27. Jeon, H.M., Lee, P.S., Bathe, K.J.: The MITC3 shell finite element enriched by interpolation covers. *Comput. Struct.* **134**, 128–142 (2014)
28. Lee, Y., Lee, P.S., Bathe, K.J.: The MITC3+ shell element and its performance. *Comput. Struct.* **138**, 12–23 (2014)
29. Jeon, H.M., Lee, Y., Lee, P.S., Bathe, K.J.: The MITC3+ shell element in geometric nonlinear analysis. *Comput. Struct.* **146**, 91–104 (2015)
30. Mathisen, K., Okstad, K.: Interactive-adaptive geometrically nonlinear analysis of shell structures. *Eng. Comput.* **12**, 63–83 (1996)
31. Li, L.M., Li, D.Y., Peng, Y.H.: The simulation of sheet metal forming processes via integrating solid-shell element with explicit finite element method. *Eng. Comput.* **27**, 273–284 (2011)
32. Sorger, C., Frischmann, F., Kollmannsberger, S., Rank, E.T.U.M.: GeoFrame: automated high-order hexahedral mesh generation for shell-like structures. *Eng. Comput.* **30**, 41–56 (2014)
33. Areias, P., de Sá, J.M.C., Cardoso, R.: A simple assumed-strain quadrilateral shell element for finite strains and fracture. *Eng. Comput.* **31**(4), 1–19 (2014)
34. Zhang, A., Ming, F., Cao, X.: Total Lagrangian particle method for the large-deformation analyses of solids and curved shells. *Acta Mech.* **225**, 253–275 (2014)
35. Nguyen-Van, H., Nguyen-Hoai, N., Chau-Dinh, T., Tran-Cong, T.: Large deflection analysis of plates and cylindrical shells by an efficient four-node flat element with mesh distortions. *Acta Mech.* **226**, 2693–2713 (2015)
36. Avramov, K.V.: Nonlinear modes of vibrations for simply supported cylindrical shell with geometrical nonlinearity. *Acta Mech.* **223**, 279–292 (2012)
37. Eliseev, V.V., Vetyukov, Y.M.: Finite deformation of thin shells in the context of analytical mechanics of material surfaces. *Acta Mech.* **209**, 43 (2009)
38. Pai, P.F.: Total-Lagrangian formulation and finite-element analysis of highly flexible plates and shells. *Math. Mech. Solids* **12**, 213–250 (2007)
39. Klinkel, S., Gruttmann, F., Wagner, W.: A mixed shell formulation accounting for thickness strains and finite strain 3D material models. *Int. J. Numer. Methods Eng.* **74**, 945–970 (2008)
40. Velčić, I.: Shallow-shell models by Γ -convergence. *Math. Mech. Solids* **17**, 781–802 (2012)
41. Birsan, M., Neff, P.: Existence of minimizers in the geometrically non-linear 6-parameter resultant shell theory with drilling rotations. *Math. Mech. Solids* **19**, 376–397 (2014)
42. Pruchnicki, E.: Two-dimensional model for the combined bending, stretching and shearing of shells: a general approach and application to laminated cylindrical shells derived from three-dimensional elasticity. *Math. Mech. Solids* **19**, 491–501 (2014)
43. Pruchnicki, E.: A fifth-order model for shells which combines bending, stretching and transverse shearing deduced from three-dimensional elasticity. *Math. Mech. Solids* **21**, 842–855 (2016)
44. Evkin, A., Kolesnikov, M., Prikazchikov, D.A.: Buckling of a spherical shell under external pressure and inward concentrated load: asymptotic solution. *Math. Mech. Solids* **22**(6) (2016)

-
45. Karasev, A.G.: Initial imperfection influence on the buckling load of closed elastic isotropic shallow conical shells. *Math. Mech. Solids* **21**, 444–453 (2016)
 46. Nachbagaer, K., Gruber, P.G., Vetyukov, Y., Gerstmayr, J.: A spatial thin beam finite element based on the absolute nodal coordinate formulation without singularities, pp. 909–917 (2011)
 47. Vetyukov, Y.: Finite element modeling of Kirchhoff-Love shells as smooth material surfaces. *ZAMM J. Appl. Math. Mech./Z. Angew. Math. Mech.* **94**, 150–63 (2014)
 48. Sze, K.Y., Liu, X.H., Lo, S.H.: Popular benchmark problems for geometric nonlinear analysis of shells. *Finite Elem. Anal. Des.* **40**, 1551–69 (2004)